

A systematic observational study of radio properties of H₂O megamaser Seyfert-2 galaxies

Z.W. Liu,¹ J.S. Zhang,^{1*} C. Henkel,^{2,3} J. Liu,⁴ P. Müller,² J.Z. Wang⁵
Q. Guo,⁶ J. Wang¹ and J. Li⁵

¹Center For Astrophysics, Guangzhou University, Guangzhou 510006, China

²Max-Planck-Institut für Radioastronomie, Auf dem Hügel 69, D-53121 Bonn, Germany

³Astronomy Department, King Abdulaziz University, P.O. Box 80203, Jeddah 21589, Saudi Arabia

⁴Xinjiang Astronomical Observatory, CAS, 150, Science 1-Street, Urumqi, Xinjiang 830011, China

⁵Shanghai Astronomical Observatory, CAS, 80, Nandan Road, Shanghai 200030, China

⁶Hunan Institute of Humanities, Science and Technology, Loudi 417000, China

Accepted XXX. Received YYY; in original form ZZZ

ABSTRACT

A systematic study is performed on radio properties of H₂O megamaser host Seyfert 2 galaxies, through multi-band radio continuum observations (at 11 cm, 6.0 cm, 3.6 cm, 2.0 cm and 1.3 cm) with the Effelsberg 100-m radio telescope within a total time duration of four days. For comparison, a control Seyfert 2 galaxy sample without detected maser emission was also observed. Spectral indices were determined for those sources for which measurements exist at two adjacent bands assuming a power-law dependence $S_\nu \propto \nu^{-\alpha}$, where S is the flux density and ν is the frequency. Comparisons of the radio continuum properties between megamaser and non-masing Seyfert 2s show no difference in spectral indices. However, a difference in radio luminosity is statistically significant, i.e. the maser galaxies tend to have higher radio luminosities by a factor of 2 to 3 than the non-masing ones, commonly reaching values above a critical threshold of $10^{29} \text{ erg s}^{-1} \text{ Hz}^{-1}$. This result confirms an earlier conclusion by Zhang et al. (2012), but is based on superior data with respect to the time interval within which the data were obtained, with respect to the observational facility (only one telescope used), the number of frequency bands.

Key words: Masers – galaxies: active – galaxies: nuclei – radio lines: galaxies – radio continuum: galaxies

1 INTRODUCTION

Great efforts have been made to study H₂O masers in extragalactic systems at $\lambda \sim 1.35 \text{ cm}$ (22.23508 GHz) in the J_{K_aK_c} = 6₁₆-5₂₃ transition, since the first detection of such an extragalactic maser towards M33 (Churchwell et al. 1977). To date, the maser line has been detected in over 160 galaxies (see the Megamaser Cosmology Project (MCP), <https://safe.nrao.edu/wiki/bin/view/Main/MegamaserCosmologyProjectwebpages>). These masers could be categorized by two classes to be associated with: (1) star formation regions (2) active galactic nuclei (AGN) (e.g. Henkel et al. 2004; Zhang et al. 2006). Among AGN-related masers, more than 30 sources have been identified as “disk-maser” candidates (Kondratko et al. 2006; Zhang et al. 2010; Greene et al. 2016; the MCP webpage). The maser

features in “disk-maser” systems trace a thin, edge-on Keplerian disk on sub-parsec scales around the central supermassive black hole (SMBH), which provides an excellent tool for accurate determinations of the black hole mass and the Hubble constant.

Observations and studies show that extragalactic H₂O masers with an isotropic luminosity greater than $10 L_\odot$, which are termed “megamasers”, are mostly found in galaxies that are categorized as Seyfert 2 or LINER (Low Ionization Nuclear Emission-Line Region) galaxies. These are heavily obscured with gas column densities $N_H > 10^{23} \text{ cm}^{-2}$ (Braatz et al. 1997; Zhang et al. 2006; Greenhill et al. 2008). A small number of sources which have been studied with high spatial resolution strongly indicate that all megamasers are AGN related. Population inversion for the H₂O 6₁₆-5₂₃ line can be explained by collisional pumping with the AGN being considered to be the ultimate energy source that feeds the maser emission (Lo 2005).

* E-mail: jszhang@gzhu.edu.cn

Potentially required "seed" photons for the maser medium aligned with the nucleus or associated with a nuclear jet may be provided by radio emission from the nucleus or jet, which would then be amplified by the maser medium, leading to strong detectable H₂O profiles. On the other side, the isotropic luminosity of the nuclear radio continuum is believed to be an indicator of AGN power (Giuricin et al. 1990; Diamond-Stanic et al. 2009). Thus we expect some kind of correlation between the isotropic luminosities of megamasers and the nuclear radio emission.

This was firstly investigated by Zhang et al. (2012). Based on collected data at 20 cm and 6.0 cm, they have proposed that maser host galaxies have higher nuclear radio continuum luminosities, exceeding those of a comparison sample by factors of order 5. Therefore nuclear radio luminosity was suggested to be a suitable indicator to guide future AGN maser searches. However, the uncertainties of that analysis are still quite high. For both maser galaxies and non-masing galaxies, measured radio data commonly come from different telescopes. Even if data could be taken from the same telescope, measurements were normally performed at different epochs. In addition, there are just a few data at other radio bands for maser host galaxies, e.g., 3.6 cm, 2.0 cm. So a presentation of a more complete dataset is urgently needed. While an interferometric study would be a better choice, systematic studies of the lower resolution radio continuum with single-dish telescopes are still worthwhile, because they are not affected by missing flux and can guide future megamaser surveys. Thus we conducted systematic Effelsberg multi-band observations toward the H₂O megamaser host galaxies and a control galaxy sample devoid of detected maser emission.

2 THE SAMPLE

As mentioned above, most maser host galaxies are Seyfert 2s or LINERs. Thus Seyfert 2 galaxies from the megamaser sample and a control sample are chosen to be our targets. Among 85 published H₂O maser galaxies, there are 49 Seyfert 2 sources. For the control Seyfert galaxy sample, we consider a complete sample consisting of 89 relatively nearby Seyfert galaxies compiled by Diamond-Stanic et al. (2009), which was drawn from the revised Shapley-Ames (RSA) catalog that selects galaxies having $B_T < 13.31$ mag (Maiolino & Rieke 1995; Ho et al. 1997). This control Seyfert sample is unique, in that it has been searched for H₂O maser emission. 54 of the 89 galaxies are Sy2s, which provide a good comparison sample (see details in Zhang et al. 2012). Among both the megamaser (49 sources) and the nonmaser (54 sources) Seyfert 2 sample, 35 masers and 25 non-masing sources with Declination > -20 degrees were observed with the Effelsberg telescope. All 35 maser sources are AGN-related and 15 of them are possibly disk-masers (Zhang et al. 2010; Kuo et al. 2011; Pesce et al. 2016).

3 OBSERVATION AND DATA REDUCTION

The multi-band radio continuum (11 cm, 6.0 cm, 3.6 cm, 2.0 cm and 1.3 cm) observations were performed on 18 to

21 January, 2014, with the Effelsberg 100-m radio telescope of the Max-Planck-Institut für Radioastronomie (MPIfR), using secondary focus heterodyne receivers. All of the flux measurements were done in cross-scan mode, where the antenna beam pattern was driven repeatedly in azimuth and elevation over the source position, switching between our targets and calibrators. Our targets were observed one by one and each source was observed in all bands within one hour, with a typical total interval time of ~ 40 minutes.

The calibration for each wavelength was obtained with the following procedure. First, baseline subtraction and Gaussian profile fitting were performed to each individual sub-scan. The amplitude of the profile provides an estimate of the source's flux density expressed in units of antenna temperature (K), divided by the signal from the noise diode. Then the Gaussian amplitude, offset and half power beam width (HPBW) of the sub-scans were independently averaged in each driving direction. The typical pointing error for the Effelsberg radio telescope is ~ 2 arcseconds, which will result in a flux density underestimation of $\sim 2\%$. However, this can be corrected by pointing correction which assumes a two dimensional Gaussian intensity profile. Subsequently, the pointing-error corrected amplitudes from both scanning directions were averaged together, providing a single flux density measurement per scan. After this, an opacity correction was made for each scan deduced from the obtained system temperature (T_{sys}). Next the systematic elevation-dependent gain variations were corrected by a polynomial function derived from non-variable calibrator sources (e.g., 3C48, 3C286, 3C295 and 3C138). Then the time-dependent gain fluctuations, which are mainly caused by changing weather conditions, were corrected by a gain-time transfer function obtained from measurements of several secondary calibrators. Finally the measured antenna temperatures (in K) of each source were converted to flux densities (in Jy), by using primary calibrator measurements (e.g. Baars et al. 1977; Ott et al. 1994). The final flux density uncertainty is composed of the statistical errors from the Gaussian fit, the weighted average over the sub-scans, the gain and time-dependent corrections, and a contribution from the residual scatter seen in the primary and secondary calibrator measurements, which characterizes uncorrected residual effects. The relative error seldom reaches up to 10% for target sources and 2% for calibrators. Figure 1 shows one example characterizing our sample of observed sources. The profiles of cross-scans of other sources are shown in the Appendix.

The above described cross-scan data calibration technique is well established and allows for high precision flux density determination (e.g. Kraus et al. 2003; Fuhrmann et al. 2008).

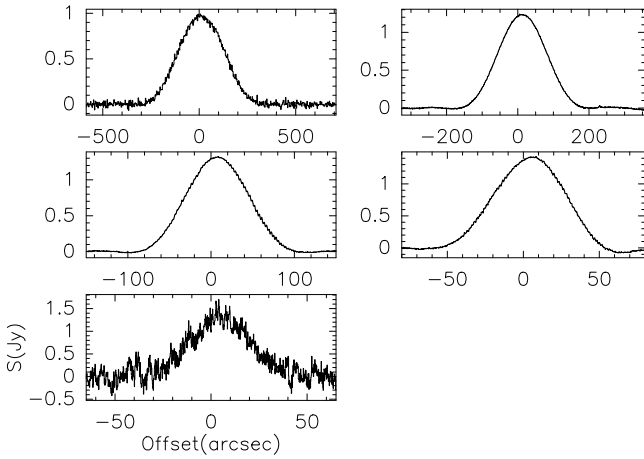
4 ANALYSIS AND DISCUSSION

4.1 Comparison of radio luminosities of H₂O maser and non-masing galaxies

Among the 35 H₂O megamaser Seyfert 2 galaxies, 24 sources ($\sim 68.6\%$) are detected at 11 cm, 25 sources ($\sim 71.4\%$) at 6.0 cm, 21 sources (60%) at 3.6 cm, 10 sources ($\sim 28.6\%$) at 2.0 cm and 2 ($\sim 5.7\%$) at 1.3 cm. Among the 25 non-masing Seyfert 2s, 16 sources (64.0%) are detected at 11 cm,

Table 1. The comparison of radio properties of megamaser and non-masing Seyfert 2s

Samples	Subsamples	$\log L_{11}$	$\log L_{6.0}$	$\log L_{3.6}$ ($\text{erg}\cdot\text{s}^{-1}\text{Hz}^{-1}$)	$\log L_{2.0}$	$\log L_{1.3}$	$\alpha_{6.0}^{11}$	$\alpha_{3.6}^6$	$\alpha_{2.0}^{3.6}$	$\alpha_{1.3}^{2.0}$
Maser	Total	29.49 ± 0.02	29.18 ± 0.01	29.02 ± 0.02	29.35 ± 0.04	30.09 ± 0.03	1.02 ± 0.14	0.96 ± 0.11	-0.12 ± 0.26	-0.27 ± 0.31
	D<70Mpc	29.34 ± 0.01	29.05 ± 0.01	28.92 ± 0.02	29.27 ± 0.03	30.09 ± 0.03	0.95 ± 0.13	0.95 ± 0.14	0.24 ± 0.19	-0.27 ± 0.31
non-masing	Total	28.71 ± 0.02	28.35 ± 0.02	28.35 ± 0.03	28.41 ± 0.03	-	1.01 ± 0.16	1.01 ± 0.17	-0.02 ± 0.25	-
	D<70Mpc	-	-	-	-	-	-	-	-	-
t-Test Prob.	Total	< 0.001	< 0.001	0.006	0.013	-	0.787	0.788	-	-
	D<70Mpc	0.007	0.003	0.027	0.068	-	-	-	-	-
Logrank-Prob.	Total	< 0.001	< 0.001	0.009	0.170	-	0.178	0.457	-	-
	D<70Mpc	0.007	0.002	0.049	0.420	-	-	-	-	-

**Figure 1.** Continuum cross scans of NGC1052 at 11 cm and 6.0 cm (top), 3.6 cm and 2.0 cm (intermediate) and 1.3 cm (bottom), respectively. For the other sources, see the Appendix.

17 sources (68%) at 6.0 cm, 11 sources (44.0%) at 3.6 cm, and 4 sources (16.0%) at 2.0 cm while no sources at 1.3 cm have been measured with signal-to-noise ratios larger than three (for details, please refer to Tables 4 and 5, upper limits are given for the flux density of those undetected sources).

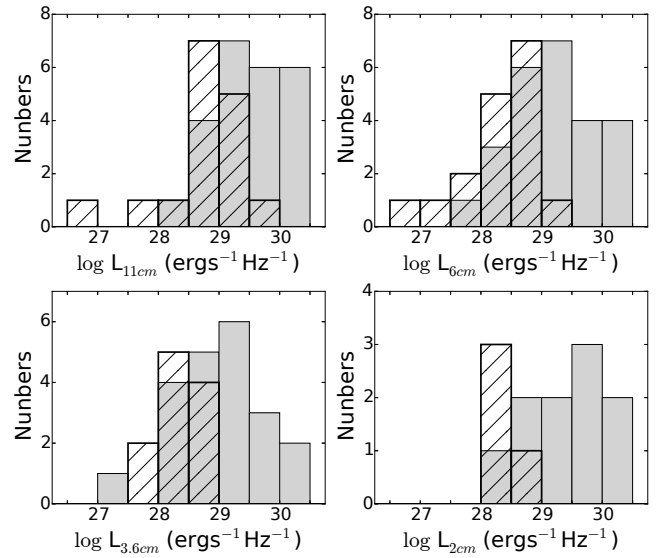
The corresponding luminosity of each individual source at each band, assuming here and elsewhere isotropic emission, are calculated by

$$L_\nu = 4\pi D^2 S_\nu, \quad (1)$$

where D is the distance of a source and S_ν is the flux density. Assuming $H_0 = 70 \text{ km s}^{-1} \text{ Mpc}^{-1}$, $\Omega_M = 0.270$ and $\Omega_{\text{vac}} = 0.730$ (e.g., Spergel et al. 2003), the distance is calculated with Cosmology Calculator I provided by the NASA Extragalactic Database (Wright 2006). The mean luminosities at each band on logarithmic scales (hereafter $\log L_{11\text{cm}}$, $\log L_{6.0\text{cm}}$, $\log L_{3.6\text{cm}}$ and $\log L_{2.0\text{cm}}$; these are given in units of $\text{erg}\cdot\text{s}^{-1}\text{Hz}^{-1}$) are listed in Table 1.

Below, we first assume that the galaxies of the maser and the control samples are, with respect to all their properties except maser and radio continuum luminosities, identical. After comparing continuum luminosities of masing and non-masing targets in this way, we will take a deeper look into the properties of the two galaxy samples and will evaluate in how far potential differences will modify our previously obtained conclusions.

The mean radio continuum luminosities for maser Seyfert 2s that are detected are $\log L_{11\text{cm}} = 29.49 \pm 0.02$, $\log L_{6.0\text{cm}} = 29.18 \pm 0.01$, $\log L_{3.6\text{cm}} = 29.02 \pm 0.02$, $\log L_{2.0\text{cm}} = 29.35 \pm 0.04$ and $\log L_{1.3\text{cm}} = 30.09 \pm 0.03$,

**Figure 2.** Distributions of radio continuum luminosities (logarithmic scales, in units of $\text{erg}\cdot\text{s}^{-1}\text{Hz}^{-1}$) at 11 cm (upper left panel), 6.0 cm (upper right), 3.6 cm (lower left) and 2.0 cm (lower right), for Seyfert 2s (grey: maser sources; open histograms with diagonal lines: sources without detected masers).

and those of the non-masing Seyfert 2s are $\log L_{11\text{cm}} = 28.71 \pm 0.02$, $\log L_{6.0\text{cm}} = 28.35 \pm 0.02$, $\log L_{3.6\text{cm}} = 28.35 \pm 0.03$ and $\log L_{2.0\text{cm}} = 28.41 \pm 0.03$, respectively (throughout the paper, given errors are the standard deviations of the mean). By comparison, the H_2O maser sources tend to possess larger mean radio continuum luminosity, with a luminosity ratio of about 6.0 ± 1.4 , 6.8 ± 1.6 , 4.7 ± 1.1 and 8.7 ± 2.0 at 11 cm, 6.0 cm, 3.6 cm and 2.0 cm, respectively. Furthermore, Welch's t-Tests were used here to check the difference of luminosity means between the entire maser and non-masing Seyfert2 samples at each band. The Welch's t-Test results (see details in Table 1, row 4) show that the difference of the luminosity means is significant at 11 cm, 6.0 cm and 3.6 cm, with a chance probability less than 0.05 (at 2.0 cm, the non-masing sample of four sources is too small to provide a reliable statistical result).

The luminosity distributions of the four bands (11 cm, 6.0 cm, 3.6 cm and 2.0 cm) are plotted in Fig.2 for both the maser sample (in grey filled histograms) and the non-masing sample (open histograms with slashes), respectively, all with a logarithmic bin size of 0.5 dex, based on $\text{erg}\cdot\text{s}^{-1}\text{Hz}^{-1}$ units. A comparison between luminosity distributions of maser and non-masing samples at each of the four bands shows the same trend: maser host galaxies have larger radio luminos-

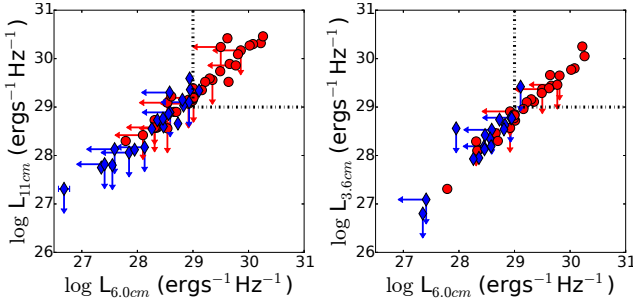


Figure 3. Radio continuum luminosity (on logarithmic scales) at 6.0 cm vs. 11 cm (left panel) and 3.6 cm (right panel). Red filled circles: maser sources. Blue filled diamonds: non-masing sources.

ity, with an intersecting region present to some extent. Since upper flux density limits could be derived for undetected sources, survival analysis was performed here to investigate the difference in luminosity distributions. The logrank test results (listed in Table 1) for the entire maser and non-masing sources show that the differences of the radio continuum luminosity distributions at 11 cm, 6.0 cm and 3.6 cm are significant with a chance probability less than 0.05 in each case, while no reliable statistical result could be obtained from the 2.0 cm data due to a too small sample.

The significant difference can also be visualized by Fig.3, which plots 6 cm vs. 11 cm (left panel) and 6 cm vs. 3.6 cm (right panel) luminosities for both maser (red circles) and non-masing (blue diamonds) Seyfert 2 sources, respectively. It demonstrates that most maser Seyfert 2 sources are located in the upper right region, at a higher luminosity, while the non-masing Seyfert 2 sources are located in the lower left, though there are a few overlaps. Together, the H₂O maser sources generally have higher radio luminosities than those of non-masing galaxies, almost an order of magnitude larger, meaning that H₂O megamasers are more likely to be found toward Seyfert 2 galaxies which possess larger radio luminosities. Dotted lines in Fig.3 enclose those sources with radio luminosities $L_\nu \geq 10^{29} \text{ erg.s}^{-1} \text{ Hz}^{-1}$ simultaneously at the two bands (6.0 cm and 11 cm for the left panel; 6.0 cm and 3.6 cm for the right panel, respectively). All but one of them are megamaser sources in the limited region. Nevertheless, we have to mention that the criterion $L_\nu \geq 10^{29} \text{ erg.s}^{-1} \text{ Hz}^{-1}$ is arbitrary, and the overlapping sections of the central regions of Fig.3 suggest that there is no clearly defined boundary on radio continuum luminosities for distinguishing megamaser and non-masing Seyfert 2 galaxies. However, choosing specifically $L_\nu \geq 10^{29} \text{ erg.s}^{-1} \text{ Hz}^{-1}$ sources would drastically improve chances for detection.

Since the brightness of an object that is observed will decrease with its distance, sources at distances where the brightness falls below the observational threshold will be unobservable. The farther the celestial objects we observe, the higher the observational threshold, which results in a severe bias in statistical evaluations (Wall & Jenkins 2012). The mean values of distances are 62.226 Mpc and 26.876 Mpc for the maser and non-masing sources, respectively. This results in a distance bias of order $(62.226/26.876)^2 \sim 5.36$. For these reasons, we eliminated all sources with $D > 70$ Mpc to acquire a minimum value of distance bias. This requires to reject 11 out of 35 maser sources, while none of the non-

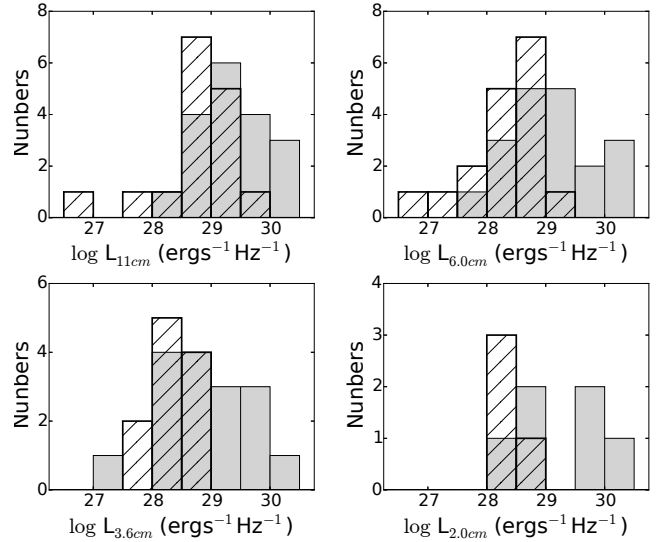


Figure 4. Distributions of the 11 cm (upper left panel), 6.0 cm (upper right panel), 3.6 cm (lower left panel) and 2.0 cm (lower right panel) radio continuum luminosity for Seyfert 2s with distance $D < 70$ Mpc (grey: maser sources and open histograms with diagonal lines: sources without detected masers).

masing sources had to be taken out. The mean distances of the maser subsample with $D < 70$ Mpc and the sample devoid of detected masers become 36.874 Mpc and 26.876 Mpc, respectively, with a distance bias of order $(36.874/26.876)^2 \sim 1.88$.

After accounting for the distances, there are small changes in mean values of luminosity for the maser subsample (for details, see Table.1), while there are no changes for the non-masing sample. The differences between both samples in radio continuum luminosity become smaller but are still obvious, with luminosity ratios of 4.3 ± 1.0 , 5.0 ± 1.2 , 3.7 ± 0.9 and 7.2 ± 1.7 for $L_{11\text{cm}}$, $L_{6.0\text{cm}}$, $L_{3.6\text{cm}}$ and $L_{2.0\text{cm}}$, respectively.

The distributions of $\log L_{11\text{cm}}$, $\log L_{6.0\text{cm}}$, $\log L_{3.6\text{cm}}$ and $\log L_{2.0\text{cm}}$ for the maser subsample (grey filled histograms) and non-masing sample (open histograms with diagonal lines) are plotted in Fig.4. The logrank test results show that the difference of the radio continuum luminosity distribution at 11 cm, 6.0 cm and 3.6 cm is still significant with a chance probability less than 0.05. Within a similar distance range ($D < 70$ Mpc), the H₂O maser sources still have larger radio luminosity means than the non-masing ones, which is further supported by t-Test results. And considering the distance bias of order ~ 1.88 , the luminosity ratios become a factor of 2 to 3.

Over all, maser host Seyfert 2 galaxies have relatively higher radio continuum luminosities than those of non-masing Seyfert 2s which agrees with the proposition that the radio luminosity is a suitable indicator to guide future AGN maser searches (Zhang et al. 2012).

4.2 Spectral properties

Assuming a power-law dependence, which is given by $S \propto \lambda^\alpha$, the spectral index between two wavelengths λ_1 and λ_2

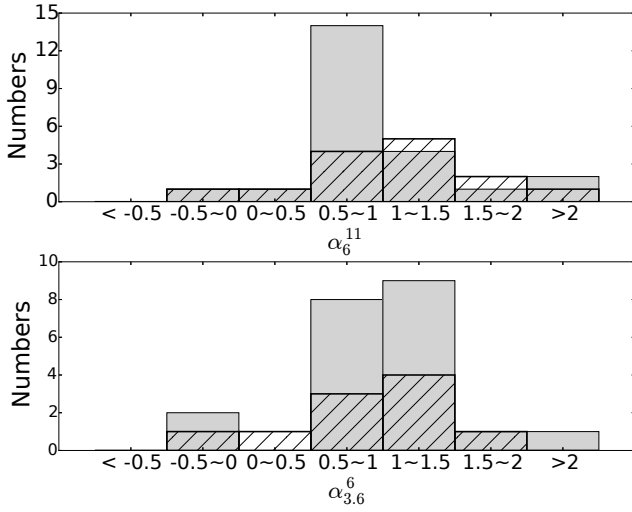


Figure 5. The distributions of radio spectral indices of Seyfert2s (grey: maser sources; open histograms with diagonal lines: sources without detected masers). Upper panel: Spectral index between 11cm and 6cm (α_6^{11}); lower panel: Spectral index between 6cm and 3.6cm ($\alpha_{3.6}^6$).

for a source can be calculated by:

$$\alpha_{\lambda_1}^{\lambda_2} = \log(S_{\lambda_1}/S_{\lambda_2})/\log(\lambda_1/\lambda_2) \quad (2)$$

The spectral indices were calculated for both our maser and non-masing Seyfert 2 sources, of which flux densities of two adjacent bands were measured, and are listed in Table 4 (see columns 10 to 13), and in Table 5 (see columns 8 to 10), respectively. Mean values are listed in Table 1.

Here, we just made statistical comparisons on α_6^{11} and $\alpha_{3.6}^6$ for our samples, since the number of sources for $\alpha_2^{3.6}$ and $\alpha_{1.3}^2$ are too small (e.g., only four maser sources with effective $\alpha_2^{3.6}$). For our maser Seyfert 2 sample, the mean values of α_6^{11} and $\alpha_{3.6}^6$ are 1.02 ± 0.14 and 0.96 ± 0.11 , respectively. And for our non-masing Seyfert 2 sample, the mean values of α_6^{11} and $\alpha_{3.6}^6$ are 1.01 ± 0.16 and 1.01 ± 0.17 , respectively. Comparisons show no significant differences in the mean values of both spectral indices between the maser and non-masing Seyfert 2 samples, which is further supported by t-Test results (listed in Table 1). Fig.5 shows the histograms of α_6^{11} and $\alpha_{3.6}^6$ for both megamaser and non-masing samples. Within the histograms, similar distributions could be found between megamaser and non-masing sources for both spectral indices, which peaks around the 0.5-1.0 bin. This is further supported by our KS-Test results (see details in Table 2), i.e., no significant difference on α_6^{11} and $\alpha_{3.6}^6$ between megamaser and non-masing Seyfert 2 galaxies. This is consistent with our previous study on α_{20}^6 for both megamaser and non-masing samples (Zhang et al. 2012). There are slight changes in mean values of α_6^{11} and $\alpha_{3.6}^6$ after accounting for the distances, and comparisons only including sources at $D < 70$ Mpc give a very similar picture.

We have plotted the mean spectral energy distribution (SED) for our maser and non-masing Seyfert 2 samples in Fig.6. The numbers of sources that are used to derive mean flux densities ($\log S$) are added to each point in the diagram. The mean flux densities are the upper limits of the whole sample in each frequency. From the figure, the mean SED

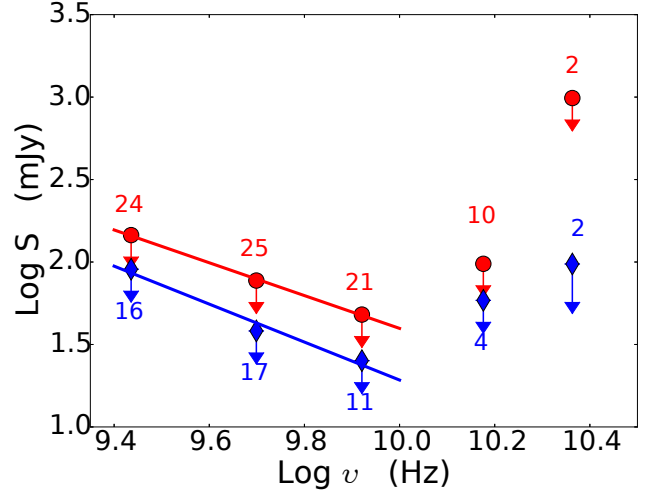


Figure 6. The mean spectral energy distribution for the maser Seyfert 2 sample (red circles) and the non-masing Seyfert 2 sample (blue diamonds). The numbers of sources that are used to derive mean flux densities ($\log S$) were added to each point in the diagram. Trend lines for mean flux densities at low frequencies (i.e. 11 cm, 6.0 cm and 3.6 cm) are presented for both samples (red line: maser Seyfert 2 sample; blue: non-masing Seyfert 2 sample).

for both samples look similar. The same downtrend is apparent at low frequency bands (i.e. 11 cm, 6.0 cm and 3.6 cm) for both Seyfert 2 samples. With slopes of -0.99 ± 0.03 and -1.15 ± 0.17 for the maser and the non-masing Seyfert 2 sample, respectively, the trend lines at the low frequency bands show that the mean flux density of Seyfert 2 galaxies decreases with frequency, which is consistent with the results of our previous work (Zhang et al. 2012). However, for both samples at high frequency (i.e., 2.0 cm and 1.3 cm), the mean flux density increases for both samples. The very low detection rate due to high noise levels in high frequency bands could account for the reversal in the mean SEDs. Observations at high frequency bands were subjected to a harsh selection effect, so that only a few bright sources could be detected with S/N larger than 3, e.g., for non-masing sources, only four sources were detected at 2 cm and there was no detection at 1.3 cm. This leads to the rather large mean flux density and ascendant trend in high frequency bands. More sensitive observations in the higher frequency bands are needed, especially for the K-band ($\lambda \sim 1.3$ cm). Another striking feature in Fig.6 is that the mean flux density of the maser Seyfert 2 sample is constantly larger than those of the non-masing ones at each band, roughly by a factor of 2. This is related to the difference in average luminosity, discussed in Sect.4.1.

4.3 Radio continuum power versus H_2O megamaser power

Since AGNs are considered to be the ultimate energy source for the H_2O megamaser emissions (Lo 2005), we may then expect to find some correlations between the power of the radio continuum and the H_2O megamaser emissions. For our megamaser Seyfert 2 sample, the apparent luminosity of H_2O megamaser emission is plotted against $\log L_{11cm}$ (upper left panel), $\log L_{6.0cm}$ (upper right panel), $\log L_{3.6cm}$ (lower

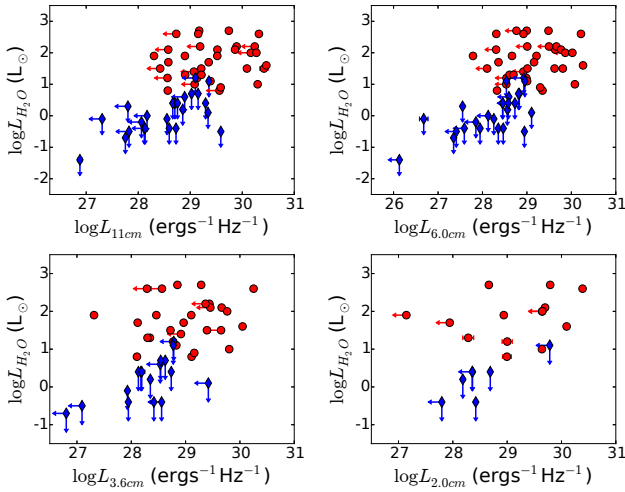


Figure 7. H_2O maser luminosities (logarithmic scale in units of L_\odot) vs. radio luminosities (logarithmic scale in units of $\text{erg}\cdot\text{s}^{-1}\text{Hz}^{-1}$) of maser host galaxies (red circles) at 11 cm (upper left panel), 6.0 cm (upper right panel), 3.6 cm (lower left panel) and 2.0 cm (lower right panel), respectively. For comparison, estimated 5σ upper limits of H_2O maser luminosity ($\log L_{\text{H}_2\text{O}}$, in units of L_\odot) of non-masing galaxies (blue diamonds) are also plotted.

Table 2. Statistical results on radio luminosity and H_2O maser luminosity for megamaser Seyfert 2s

	11 cm	6.0 cm	3.6 cm	2.0 cm
Spearman's Coeff.	0.13	0.06	0.31	0.24
Spearman's Prob.	0.54	0.77	0.18	0.51

Note: the values are calculated from linear fits in four frequency bands. A positive coefficient indicates a positive correlation implying that radio luminosity and H_2O luminosity for megamaser Seyfert 2s tend to increase together. A correlation coefficient is significant if probability is less than the significance level of 0.05.

left panel) and $\log L_{2.0\text{cm}}$ (lower right panel) in Fig. 7. Assuming a linewidth of 20 km s^{-1} , 5σ upper limits of H_2O maser luminosity are derived from the individual rms values (taken from the MCP website, as mentioned in Sect. 1) of H_2O maser data for the non-masing Seyfert 2s (e.g., Bennert et al. 2009). For comparison, these upper limits (details in Table 5) are also plotted in Fig. 7. Owing to the low number of detections, the luminosity of the radio continuum in the 1.3 cm band is not part of the following discussion.

From Fig. 7, it is apparent that H_2O undetected sources tend to locate in the lower left region and maser sources in the upper right region, which is consistent with our previous results. For the megamaser sample alone, there is no significant correlation between luminosities of the H_2O megamaser emission and the radio continuum, which is supported by Spearman's rank tests. The results listed in Table 2 indicate that there could be a positive but statistically weak correlation at each band. This is consistent with previous results of Zhang et al. (2012). Adopting the scenario that the H_2O maser emission is mainly produced by amplification of the nuclear radio continuum emission, the lack of a correlation should be mainly caused by large uncertainties on both luminosities.

Uncertainties in H_2O maser luminosity possibly may

arise from directional maser emission and different AGN related maser types (Zhang et al. 2012). For uncertainties in nuclear radio luminosity, two possible causes should be considered. First, uncertainties may be introduced assuming the measured radio continuum luminosity as isotropic indicator of the intrinsic AGN power, since the observed radio power possibly depends on the AGN torus structure (Zhang et al. 2012). Another effect, which may be relevant here, is that the observed nuclear radio power could be contaminated by the large scale emission of the host galaxy (Diamond-Stanic et al. 2009). The beam size of the Effelsberg 100 m radio telescope at our observed bands is at least $40''$, which corresponds to a linear size of $\sim 2\text{ kpc}$ for a source at distance 10 Mpc. This is much larger than that of the maser spots observed on sub-pc scales (e.g., Miyoshi et al. 1995; Reid et al. 2009) and that of potentially associated nuclear continuum sources. Systematic interferometric observations with high resolution are required to resolve the scenario between nuclear continuum and maser spot distribution.

4.4 Constraints on parameters of H_2O megamaser AGNs?

Based on the fact that megamaser Seyfert 2s tend to have larger radio continuum luminosities (with robust limits of $L_\nu \geq 10^{29}\text{ erg}\cdot\text{s}^{-1}\text{Hz}^{-1}$, see Sect. 4.1), we try to investigate possible constraints on AGN parameters of H_2O megamaser hosts. For both our Seyfert 2 samples, we compiled mean stellar velocity dispersions of 20 out of 35 megamaser sources and 24 out of 25 non-maser ones from HyperLeda (<http://leda.univ-lyon1.fr/>). For an additional seven megamaser sources, their stellar velocity dispersions are taken from the literature (see details in Table 6). The corresponding BH masses for each source are calculated with the $M-\sigma$ relation

$$\log\left(\frac{M_{\text{BH}}}{M_\odot}\right) = \alpha + \beta \log\left(\frac{\sigma}{200\text{ km s}^{-1}}\right), \quad (3)$$

where $\alpha = 8.08$ and $\beta = 4.47$ (Gültekin et al. 2009). Here we have to mention, the $M_{\text{BH}}-\text{Sigma}$ relation defined by elliptical galaxies with high mass, may not provide good BH mass estimations for low-mass maser galaxy systems, which is proposed from precise BH mass measurements from disk megamaser sources (Greene et al. 2010, 2016). For those common seven disk megamaser sources, our results from the $M-\text{Sigma}$ relation are basically consistent with their results from the dynamics of disk megamasers, with the largest differences less than 0.8 dex (see details in Table 6). Their measured BH mass results are used in our following analysis.

Number distributions of derived BH masses for maser and non-masing samples are plotted in Fig. 8. The distributions of BH masses for both (also the disk maser subsample) samples mainly range from $10^{6.5} M_\odot$ to $10^{8.5} M_\odot$ with a similar mean value of $\sim 10^{7.35} M_\odot$. A logrank test gives a p-value of 0.54 suggesting that there is no significant difference on M_{BH} distributions for our maser Seyfert 2s and the non-masing Seyfert 2s, though non-masing Seyfert 2s tend to have larger peak values.

Taken the radio continuum luminosity as an isotropic luminosity indicator of AGN power (e.g., Diamond-Stanic et al. 2009; Giuricin et al. 1990), the

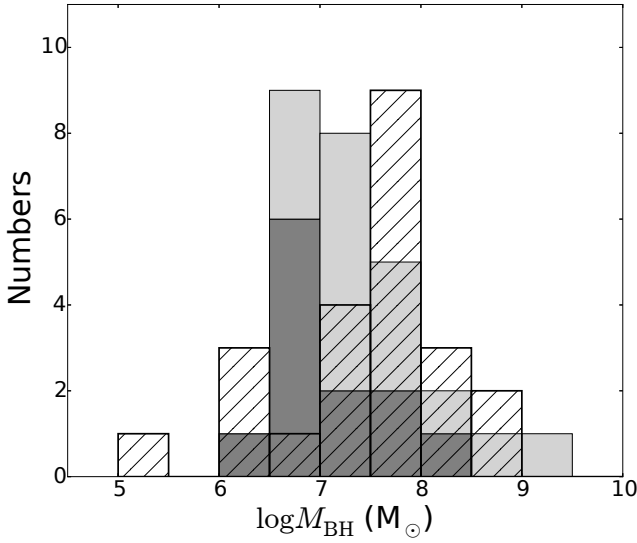


Figure 8. The distributions of derived BH masses. Dark histograms: disk maser sources. Grey histograms: maser sources of other kinds. Open histograms with diagonal lines: non-masing galaxies.

Table 3. Mean values of the dimensionless and mass accretion rates

Sample	Sub-sample	$\log \dot{m}_{11}$	$\log \dot{m}_6$	$\log \dot{M}_{11}$	$\log \dot{M}_6$
Maser	Total	-6.61 ± 0.13	-6.64 ± 0.14	-6.81 ± 0.13	-6.86 ± 0.14
	Disk-maser	-6.64 ± 0.20	-6.66 ± 0.20	-7.07 ± 0.16	-7.08 ± 0.17
Non-masing		-7.42 ± 0.19	-7.59 ± 0.16	-7.55 ± 0.16	-7.65 ± 0.15
t-Test Prob.		0.017	0.001	0.001	<0.001

Note: t-Test results for maser and non-masing samples.

dimensionless accretion rate (i.e., Eddington ratio) can be estimated:

$$\dot{m}_\nu = \frac{L_\nu}{L_{\text{Edd}}}, \quad (4)$$

where L_ν is the radio continuum luminosity and Eddington luminosities L_{Edd} are calculated from

$$L_{\text{Edd}} = 1.3 \times 10^{46} \left(\frac{M_{\text{BH}}}{10^8 M_\odot} \right) \text{erg s}^{-1}. \quad (5)$$

Adopting the standard accretion model, where within three times the Schwarzschild radius $3r_g = 3 \times \frac{2GM}{c^2}$, matter falls into the central black-hole and presumably half of the gravitational energy transforms into radiation, the mass accretion rate can be estimated by Ishihara et al. (2001):

$$\dot{M}_\nu = \frac{12L_\nu}{c^2} = 2 \times 10^{-5} \left(\frac{L_\nu}{1.0 \times 10^{41} \text{erg s}^{-1}} \right) M_\odot \text{yr}^{-1}. \quad (6)$$

Estimated values of the dimensionless \dot{m}_ν (Eq. 4) and mass accretion rates \dot{M}_ν (Eq. 6) are listed in Table 6 and 7, respectively.

Fig.9 (upper panels) presents the distributions of accretion rates for both maser and non-masing samples. It shows that the maser Seyfert 2s tend to have higher accretion rates than the non-masing ones. The mean accretion rates of maser Seyfert 2s are nearly one order of magnitude larger than those of non-masing Seyfert 2s (Table 3). No

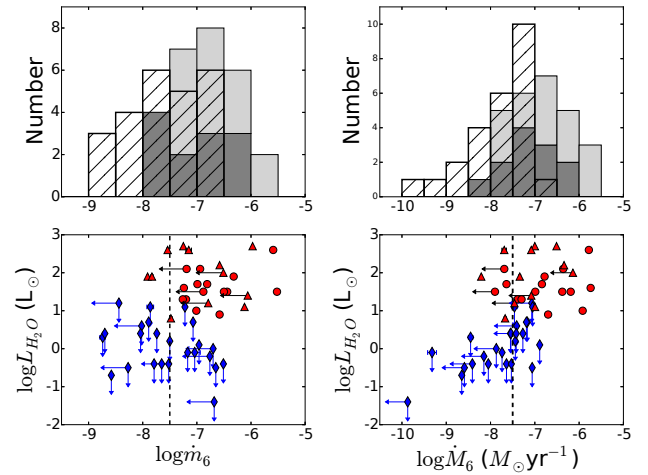


Figure 9. Upper panels: Number distributions of logarithmic accretion rates, specifically referring to $\log \dot{m}_6$ (left), defined by Eq.(4), and $\log \dot{M}_6$ (right), defined by Eq.(6). The indices indicate that the data are derived from radio continuum luminosities at 6.0 cm. Dark histograms: disk maser sources. Grey histograms: maser sources of other kinds. Open histograms with diagonal lines: non-masing galaxies. Lower panels: H_2O megamaser luminosities vs. $\log \dot{m}_6$ (left) and $\log \dot{M}_6$ (right). Circles and triangles indicate possible disk maser sources and maser sources of other kinds, respectively. Blue diamonds are non-masing sources. Dashed lines: $\log \dot{m}_6 = -7.5$ and $\log \dot{M}_6 = -7.5$.

significant difference can be found between disk-masers and other types of AGN masers.

In the lower panels of Fig.9, maser luminosities are plotted against both accretion rates that are derived from radio continuum luminosities at 6.0 cm (in logarithmic scale, $\log \dot{m}_6$ and $\log \dot{M}_6$). The difference in accretion rate between maser and non-masing samples is obvious, i.e., maser Seyfert 2s tend to possess larger accretion rates. For most of maser Seyfert 2s, the dimensionless (Eq. 4) and mass accretion (Eq. 6) rate are larger than $10^{-7.5}$ and $10^{-7.5} M_\odot \text{yr}^{-1}$, respectively (dotted lines in the lower panels of Fig.9). These agree with the limited criteria of $L_\nu \geq 10^{29} \text{erg s}^{-1} \text{Hz}^{-1}$ we proposed in Sect. 4.1, with a mean BH mass of $10^8 M_\odot$.

5 SUMMARY

In this paper, multi-band radio continuum observations from the Effelsberg 100 m telescope are presented targeting H_2O megamaser host Seyfert 2s and a control Seyfert 2 sample without maser detection. Radio properties of these two samples were compared to obtain a better understanding of intrinsic radio properties of H_2O maser host galaxies, the formation of such megamasers, and to provide a better guidance for future megamaser surveys.

Megamaser Seyfert 2 galaxies tend to possess larger radio luminosity than Seyfert 2s without maser detection. The mean radio continuum luminosities for maser Seyfert 2s that are detected are $\log L_{11\text{cm}} = 29.49 \pm 0.02$, $\log L_{6.0\text{cm}} = 29.18 \pm 0.01$, $\log L_{3.6\text{cm}} = 29.02 \pm 0.02$, $\log L_{2.0\text{cm}} = 29.35 \pm 0.04$ and $\log L_{1.3\text{cm}} = 30.09 \pm 0.03$, and those of non-masing Seyfert 2s are $\log L_{11\text{cm}} = 28.71 \pm 0.02$, $\log L_{6.0\text{cm}} = 28.35 \pm 0.02$, $\log L_{3.6\text{cm}} = 28.35 \pm 0.03$ and $\log L_{2.0\text{cm}} =$

28.41 ± 0.03 , respectively. Considering a distance bias of order ~ 1.88 , the luminosity difference remains significant, with luminosity ratios of order 2-3.

For both samples, spectral indices are derived between two adjacent bands. The mean values of α_{11cm}^{6cm} and $\alpha_{6cm}^{3.6cm}$ are 1.02 ± 0.14 , 0.96 ± 0.11 for the maser Seyfert 2 sample and 1.01 ± 0.16 , 1.01 ± 0.17 for the non-masing Seyfert 2 samples, respectively. Comparisons on distributions of spectral indices show no significant differences. Due to large uncertainties in the H_2O isotropic luminosity and radio luminosity of maser host Seyfert 2s, the statistical correlation is not obvious between them.

Overall, our results confirm the trend that H_2O maser host Seyfert 2 galaxies have larger radio luminosity than non-masing Seyfert 2s. Taking the radio luminosity as an isotropic tracer of AGN power, thus megamaser Seyfert 2s have stronger AGN power than non-masing Seyfert 2s. The black hole mass, the dimensionless and mass accretion rate were estimated for our maser Seyfert 2s and non-masing Seyfert 2s. It shows that the accretion rates of maser Seyfert 2s are nearly one order larger than non-masing Seyfert 2s. This may provide possible connection between H_2O megamaser formation and AGN activity, as well suitable constraints on future megamaser surveys.

ACKNOWLEDGEMENTS

This work is supported by China Ministry of Science and Technology under State Key Development Program for Basic Research (2012CB821800) and the Natural Science Foundation of China (No. 11473007, 11590782, 11590780, 11590784).

REFERENCES

- Baars J. W. M., Genzel R., Pauliny-Toth I. I. K., Witzel A., 1977, *Astronomy & Astrophysics*, 61, 99
- Bennert N., Barvainis R., Henkel C., Antonucci R., 2009, *The Astrophysical Journal*, 695, 276
- Braatz J. A., Wilson A. S., Henkel C., 1997, *The Astrophysical Journal Supplement Series*, 110, 321
- Churchwell E., Witzel A., Huchtmeier W., Pauliny-Toth I., Roland J., Sieber W., 1977, *Astronomy & Astrophysics*, 54, 969
- Darling J., Brogan C., Johnson K., 2008, *The Astrophysical Journal*, 685, L39
- Diamond-Stanic A. M., Rieke G. H., Rigby J. R., 2009, *The Astrophysical Journal*, 698, 623
- Fuhrmann L., et al., 2008, *Astronomy & Astrophysics*, 490, 1019
- Giuricin G., Madirossian F., Mezzetti M., Bertotti G., 1990, *Astrophysical Journal Supplement Series* (ISSN 0067-0049), 72, 551
- Greene J. E., et al., 2010, *The Astrophysical Journal*, 721, 26
- Greene J. E., et al., 2016, *The Astrophysical Journal Letters*, 826, L32
- Greenhill L. J., Tilak A., Madejski G., 2008, *The Astrophysical Journal*, 686, L13
- Gültekin K., et al., 2009, *The Astrophysical Journal*, 698, 198
- Henkel C., Braatz J. A., Tarchi A., Peck A. B., Nagar N. M., Greenhill L. J., Wang M., Hagiwara Y., 2004, *arXiv.org*, pp 107–116
- Ho L. C., Filippenko A. V., Sargent W. L. W., 1997, *The Astrophysical Journal Supplement Series*, 112, 315
- Ishihara Y., Nakai N., Iyomoto N., Makishima K., Diamond P., Hall P., 2001, *Publications of the Astronomical Society of Japan*, 53, 215
- Kondratko P. T., Greenhill L. J., Moran J. M., 2006, *The Astrophysical Journal*, 652, 136
- Kraus A., et al., 2003, *Astronomy & Astrophysics*, 401, 161
- Kuo C. Y., et al., 2011, *The Astrophysical Journal*, 727, 20
- Lo K. Y., 2005, *Annual Review of Astronomy & Astrophysics*, 43, 625
- Maiolino R., Rieke G. H., 1995, *Astrophysical Journal* v.454, 454, 95
- Miyoshi M., Moran J., Herrnstein J., Greenhill L., Nakai N., Diamond P., Inoue M., 1995, *Nature*, 373, 127
- Ott M., Witzel A., Quirrenbach A., Krichbaum T. P., Standke K. J., Schalinski C. J., Hummel C. A., 1994, *Astronomy and Astrophysics* (ISSN 0004-6361), 284, 331
- Pesce D., et al., 2016, in *American Astronomical Society Meeting Abstracts*. p. 243.59
- Reid J. S., Zhang J., Hyer E. J., Campbell J. R., Christopher S. A., Ferrare R. A., Leptoukh G. G., Stackhouse P. W., 2009, *American Geophysical Union*, 14, 08
- Spergel D. N., et al., 2003, *The Astrophysical Journal Supplement Series*, 148, 175
- Su J.-B., Zhang J.-S., Fan J.-H., 2008, *Chinese Journal of Astronomy and Astrophysics*, 8, 547
- Tarchi A., Castangia P., Columbano A., Panessa F., Braatz J. A., 2011, *Astronomy & Astrophysics*, 532, A125
- Wall J. V., Jenkins C. R., 2012, *Practical Statistics for Astronomers*
- Wang J., Zhang J. S., Guo Q., 2010, *Astronomical Research & Technology*, 7, 185
- Wright E. L., 2006, *PASP*, 118, 1711
- Zhang J. S., Henkel C., Kadler M., Greenhill L. J., Nagar N., Wilson A. S., Braatz J. A., 2006, *Astronomy & Astrophysics*, 450, 933
- Zhang J. S., Henkel C., Guo Q., Wang H. G., Fan J. H., 2010, *The Astrophysical Journal*, 708, 1528
- Zhang J. S., Henkel C., Guo Q., Wang J., 2012, *Astronomy &*

Table 4. Radio properties of H_2O megamaser Seyfert 2 galaxies

Source	Type	D	$\log L_{H_2O}$	S_{11}	S_6	$S_{3.6}$	S_2	$S_{1.3}$	α_6^{11}	$\alpha_{3.6}^6$	$\alpha_{2.6}^{3.6}$	$\alpha_{1.3}^2$
NGC 17	Sy2	79.1	0.8	<48.85	30.03 \pm 1.06	17.25 \pm 0.95	13.24 \pm 2.51	-	-	1.09	0.45	-
Mrk 348	Sy2	62	2.6	455.89 \pm 6.56	358.54 \pm 4.65	388.64 \pm 8.05	531.92 \pm 13.87	723.42 \pm 48.98	0.4	-0.16	-0.53	-0.71
Mrk 1	Sy2	25	1.7	50.86 \pm 2.89	30.69 \pm 1.48	17.55 \pm 1.13	<11.74	-	0.83	1.09	-	-
NGC 591	Sy2	61	1.4	<26.48	<18.69	<18.48	-	-	-	-	-	-
IC 0184	Sy2	70.5	1.0	<20.48	<5.78	-	-	-	-	-	-	-
NGC 1052	Sy2	17	2.1	965.5 \pm 7.75	1253.17 \pm 14.64	1334.14 \pm 26.55	1444.74 \pm 31.49	1345.92 \pm 74.55	-0.43	-0.12	-0.14	0.16
NGC 1068	Sy2	14.5	2.2	3100.99 \pm 25.47	1830.81 \pm 20.95	1092.31 \pm 22.04	-	-	0.87	1.01	-	-
NGC 1106	Sy2	57.8	0.9	96.54 \pm 2.69	49.92 \pm 1.67	36.19 \pm 1.47	-	-	1.09	0.63	-	-
Mrk 1066	Sy2	48	1.5	59.24 \pm 2.63	37.34 \pm 1.47	19.14 \pm 1.76	-	-	0.76	1.31	-	-
NGC 1320	Sy2	35.5	1.2	<24.26	<23.04	-	-	-	-	-	-	-
IRAS 0335+0104	Sy2	159.1	2.1	24.05 \pm 1.37	<19.35	<9.44	-	-	-	-	-	-
UGC 3255	Sy2	75	1.2	20.18 \pm 1.89	14.45 \pm 0.96	8.77 \pm 0.69	14.91 \pm 3.20	-	0.55	0.98	-0.9	-
Mrk 3	Sy2	54	1.0	568.04 \pm 8.74	345.02 \pm 4.27	182.56 \pm 3.94	125.25 \pm 6.81	<170.28	0.82	1.25	0.64	-
VII Zw 073	Sy2	158.9	2.2	<57.63	<10.41	<7.71	-	-	-	-	-	-
NGC 2273	Sy2	24.5	0.8	51.59 \pm 3.62	29.64 \pm 1.12	17.72 \pm 0.86	-	-	0.91	1.01	-	-
UGC 3789	Sy2	44.3	2.6	<22.99	8.73 \pm 1.01	<8.32	-	-	-	-	-	-
Mrk 78	Sy2	150	1.5	97.51 \pm 17.57	15.58 \pm 0.94	9.2 \pm 0.79	-	-	3.03	1.03	-	-
Mrk 1210	Sy2	54	1.9	95.11 \pm 2.19	47.19 \pm 1.41	36.52 \pm 1.08	24.89 \pm 2.28	-	1.16	0.5	0.65	-
NGC 2979	Sy2	36	2.1	<24.41	<13.09	-	-	-	-	-	-	-
NGC 3079	Sy2	15.5	2.7	517.99 \pm 4.68	344.51 \pm 4.11	246.19 \pm 4.95	160.33 \pm 4.11	<221.44	0.67	0.66	0.73	-
Mrk 34	Sy2	205	2.0	<29.14	<14.50	-	-	-	-	-	-	-
NGC 3393	Sy2	50	2.6	47.71 \pm 2.43	28.01 \pm 1.52	<12.3	-	-	0.88	-	-	-
NGC 3735	Sy2	36	1.3	106.17 \pm 3.81	26.22 \pm 0.99	14.24 \pm 0.89	-	-	2.31	1.2	-	-
NGC 4258	Sy1.9	7.2	1.9	324.67 \pm 4.47	98.89 \pm 2.48	33.29 \pm 0.97	<22.49	-	1.96	2.13	-	-
NGC 4388	Sy2	34	1.1	177.51 \pm 1.95	73.18 \pm 1.27	48.92 \pm 1.53	-	-	1.46	0.79	-	-
NGC 5256	Sy2	112	1.5	82.14 \pm 1.86	42.89 \pm 1.19	<30.01	-	-	1.07	-	-	-
NGC 5347	Sy2	31	1.5	<23.02	<11.08	-	-	-	-	-	-	-
NGC 5506	Sy1.9	25	1.7	303.26 \pm 3.54	193.7 \pm 2.73	123.16 \pm 2.64	-	<149.03	0.74	0.89	-	-
NGC 5728	Sy2	37	1.9	48.4 \pm 2.17	28.25 \pm 1.13	<17.68	-	-	0.89	-	-	-
NGC 5793	Sy2	47	2.0	709.73 \pm 7.48	399.52 \pm 5.03	220.84 \pm 4.77	<167.47	-	0.95	1.16	-	-
NGC 6240	Sy2	98	1.6	253.21 \pm 3.85	159.61 \pm 2.66	97.45 \pm 2.64	108.36 \pm 5.19	<144.44	0.76	0.97	-0.18	-
NGC 6323	Sy2	104	2.7	-	<4.50	-	-	-	-	-	-	-
IRAS F1937-0131	Sy2	80	2.2	<20.29	<13.31	-	-	-	-	-	-	-
NGC 6926	Sy2	80	2.7	72.41 \pm 2.42	40.02 \pm 1.08	25.31 \pm 1.47	81.06 \pm 4.92	-	0.98	0.90	-1.98	-
NGC 7479	Sy2	31.8	1.3	66.24 \pm 2.52	41.17 \pm 1.68	16.46 \pm 1.40	15.90 \pm 3.67	<165.51	0.78	1.79	0.06	-

Note: Column (1): Source name (15 out of 35 are possible disk-masers in bold text). Column (2): Types of nuclear activity from Zhang et al. (2010). Column (3): Luminosity distance in units of Mpc, assuming $H_0 = 70 \text{ km s}^{-1} \text{ Mpc}^{-1}$. NGC 17 and NGC 1320 from Greenhill et al. (2008). Column (4): Apparent luminosity of maser emission (on a logarithmic scale), in units of L_\odot , taken from Tarchi et al. (2011), Bennert et al. (2009), Greenhill et al. (2008), and Darling et al. (2008). Columns (5) to (9): Observed flux densities at 11 cm, 6.0 cm, 3.6 cm, 2.0 cm and 1.3 cm, in mJy, respectively. Column (10) to (13): Spectral indices assuming $S \propto \nu^{-\alpha}$.

Table 5. Radio properties of Seyfert 2 galaxies without H_2O maser detections

Source	Type	D	rms- H_2O	UL- H_2O	S_{11}	S_6	$S_{3.6}$	S_2	$S_{1.3}$	α_6^{11}	$\alpha_{3.6}^6$	$\alpha_{2.6}^{3.6}$
NGC 777	Sy2	66.5	6.9	1.2	<23.86	<16.14	<11.46	-	-	-	-	-
NGC 1058	Sy2	9.2	20	-0.1	<20.03	4.71 \pm 1.04	-	-	-	-	-	-
NGC 1358	Sy2	52.6	3	0.6	<23.64	<11.88	<10.35	-	-	-	-	-
NGC 1667	Sy2	61.2	6.6	1.1	51.11 \pm 2.8	20.08 \pm 1.44	13.24 \pm 0.98	<135.91	-	1.54	0.82	-
NGC 2655	Sy2	24.4	5.2	0.2	100.98 \pm 7.78	51.04 \pm 1.46	31.54 \pm 2.17	21.46 \pm 1.73	-	1.13	0.94	0.66
NGC 2992	Sy1.9	34.1	2.3	0.1	158.54 \pm 3.09	91.68 \pm 1.81	<188.82	-	-	0.9	-	-
NGC 3147	Sy2	40.9	6.3	0.7	53.04 \pm 1.74	33.73 \pm 1.11	21.11 \pm 1.55	-	-	0.75	0.92	-
NGC 3185	Sy2	21.3	3	-0.2	<21.31	<13.12	-	-	-	-	-	-
NGC 3976	Sy2	37.7	16	1.1	-	20.32 \pm 2.9	-	-	-	-	-	-
NGC 3982	Sy1.9	17	3	-0.4	37.93 \pm 2.01	25.54 \pm 1.76	<104.74	<18.15	-	0.65	-	-
NGC 4138	Sy1.9	17	2.4	-0.5	1122.88 \pm 42.71	254.58 \pm 3.38	-	-	-	2.45	-	-
NGC 4168	Sy1.9	16.8	15	0.3	<18.83	10.58 \pm 1.12	-	-	-	-	-	-
NGC 4395	Sy1.8	4.6	3.8	-1.4	29.97 \pm 3.18	<5.38	-	-	-	-	-	-
NGC 4472	Sy2	16.8	17	0.4	150.3 \pm 2.68	83.96 \pm 1.72	44.6 \pm 1.56	68.34 \pm 3.3	-	0.96	1.24	-0.73
NGC 4501	Sy2	16.8	3	-0.4	158.19 \pm 2.25	67.31 \pm 1.24	26.22 \pm 1.47	-	-	1.41	1.85	-
NGC 4565	Sy1.9	9.7	4.6	-0.7	50.41 \pm 1.72	19.94 \pm 0.97	<5.66	-	-	1.53	-	-
NGC 4579	Sy1.9	16.8	3	-0.4	117.08 \pm 2.75	87 \pm 1.38	77.37 \pm 1.82	78.32 \pm 3.59	<145.27	0.49	0.23	-0.02
NGC 4594	Sy1.9	20	13	0.4	96.65 \pm 2.14	112.34 \pm 1.78	113.87 \pm 3.29	102.27 \pm 6.58	-	-0.25	-0.03	0.18
NGC 4725	Sy2	12.4	4.1	-0.5	<36.2	<14.03	<6.76	-	-	-	-	-
NGC 4941	Sy2	16.8	3	-0.4	<40.26	<11.58	-	-	-	-	-	-
NGC 5005	Sy2	21.3	10	0.4	104.96 \pm 2.53	52.97 \pm 1.48	24.93 \pm 1.17	-	<65.15	1.13	1.48	-
NGC 5395	Sy2	46.7	4.1	0.7	54.46 \pm 1.59	24.81 \pm 1.07	13.36 \pm 1.28	-	-	1.3	1.21	-
NGC 5899	Sy2	42.8	3	0.4	90.18 \pm 4.22	<17.43	7.12 \pm 0.91	<10.39	-	-	-	-
NGC 6951	Sy2	24.1	3	-0.1	51.42 \pm 2.18	25.98 \pm 1.01	12.25 \pm 0.86	-	-	1.13	1.47	-
NGC 7743	Sy2	24.4	3	0.0	<20.80	<18.92	-	-	-	-	-	-

Note: Column (1): Source name. Column (2): Optical classification from Maiolino & Rieke (1995) or Ho et al. (1997). Column (3): Luminosity distance in units of Mpc, taken from Diamond-Stanic et al. (2009). Column (4): Rms values of H_2O maser data in units of mJy for a 20 km s^{-1} wide channel, which were taken from MPC and HoME webpages. Column(5): Estimated 5σ upper limits of H_2O maser luminosity ($\log L_{H_2O}$, in units of L_\odot) for non-masing Seyfert 2 galaxies from rms values. Columns (6) to (10): Observed flux densities at 11 cm, 6.0 cm, 3.6 cm and 2.0 cm, respectively. Columns (11) to (13): Spectral indice assuming $S \propto \nu^{-\alpha}$.

Table 6. The Parameters of 27 (out of 35) galaxies of the Megamaser Seyfert 2 sample

Source	σ	$\log M_{\text{BH}}$	$\log L_{\text{H}_2\text{O}}$	$\log L_{\text{Edd}}$	$\log \dot{m}_{11}$	$\log \dot{m}_{6.0}$	$\log \dot{M}_{11}$	$\log \dot{M}_{6.0}$
Mrk 348	141	7.40	2.6	45.51	-5.75±0.01	-5.59±0.01	-5.94 ± 0.01	-5.78 ± 0.01
Mrk 1	111	6.94	1.7	45.05	-7.03±0.02	-6.99±0.02	-7.68 ± 0.02	-7.64 ± 0.02
NGC 1052	210	8.17	2.1	46.28	-7.32±0.01	-6.94±0.01	-6.74 ± 0.01	-6.36 ± 0.01
NGC 1106	146	7.47	0.9	45.58	-6.56±0.01	-6.58±0.01	-6.68 ± 0.01	-6.70 ± 0.01
Mrk 1066	117	7.04	1.5	45.15	-6.50±0.02	-6.44±0.02	-7.05 ± 0.02	-6.99 ± 0.02
Mrk 3	273	8.68	1.0	46.79	-7.06±0.01	-7.01±0.01	-5.97 ± 0.01	-5.92 ± 0.01
Mrk 78	165	7.71	1.5	45.82	-5.97±0.08	-6.50±0.03	-5.84 ± 0.08	-6.38 ± 0.03
Mrk 1210	114	7.12	1.9	45.23	-6.27±0.01	-6.32±0.01	-6.74 ± 0.01	-6.78 ± 0.01
NGC 2979	112	7.09	2.1	45.20	<-7.19	<-7.19	<-7.69	<-7.69
NGC 3735	141	7.40	1.3	45.51	-6.86±0.02	-7.20±0.02	-7.05 ± 0.02	-7.39 ± 0.02
NGC 5256	100	6.92	1.5	45.03	-5.50±0.01	-5.52±0.01	-6.17 ± 0.01	-6.19 ± 0.01
NGC 5347	92	6.57	1.5	44.68	<-6.82	<-6.88	<-7.84	<-7.9
NGC 5506	180	7.56	1.7	45.67	-6.88±0.01	-6.81±0.01	-6.91 ± 0.01	-6.84 ± 0.01
NGC 6240	336	9.09	1.6	47.20	-7.30±0.01	-7.24±0.01	-5.80 ± 0.01	-5.74 ± 0.01
NGC 7479	152	7.55	1.3	45.66	-7.32±0.02	-7.26±0.02	-7.36 ± 0.02	-7.30 ± 0.02
Mrk 34	181	7.96	2.0	46.07	<-6.47	<-6.51	<-6.10	<-6.14
NGC 5728	200	8.08	1.9	46.19	-7.86±0.02	-7.83±0.02	-7.36 ± 0.02	-7.34 ± 0.02
NGC 6926	109	7.04	2.7	45.15	-5.97±0.01	-5.97±0.01	-6.52 ± 0.01	-6.51 ± 0.01
NGC 591	92	6.57	1.4	44.68	<-6.17	<-6.06	<-7.19	<-7.08
UGC 3789	107	7.05	2.6	45.16	<-6.99	-7.15±0.05	<-7.53	-7.69 ± 0.05
UGC 3789 (*)		6.99	2.6	45.10	<-6.93	-7.09±0.05		
NGC 1068	176	7.83	2.2	45.94	-6.61±0.01	-6.58±0.01	-6.37 ± 0.01	-6.34 ± 0.01
NGC 1068 (*)		6.92	2.2	45.03	-5.70±0.01	-5.67±0.01		
NGC 1320	110	6.92	1.2	45.03	<-7.03	<-6.79	<-7.70	<-7.46
NGC 1320 (*)		6.74	1.2	44.85	<-6.85	<-6.61		
NGC 2273	141	7.40	0.8	45.51	-7.51±0.03	-7.48±0.02	-7.70 ± 0.03	-7.67 ± 0.02
NGC 2273 (*)		6.93	0.8	45.04	-7.04±0.03	-7.01±0.02		
NGC 3079	176	7.83	2.7	45.94	-7.33±0.01	-7.25±0.01	-7.09 ± 0.01	-7.00 ± 0.01
NGC 3079 (*)		6.4	2.7	44.51	-5.9±0.01	-5.82±0.01		
NGC 3393	197	8.05	2.6	46.16	-7.57±0.02	-7.54±0.02	-7.11 ± 0.02	-7.08 ± 0.02
NGC 3393 (*)		7.2	2.6	43.31	-6.72±0.02	-6.69±0.02		
NGC 4258	133	7.29	1.9	45.40	-7.66±0.01	-7.91±0.01	-7.96 ± 0.01	-8.21 ± 0.01
NGC 4258 (*)		7.58	1.9	45.69	-7.95±0.01	-8.20±0.01		
NGC 4388	99	6.71	1.1	44.82	-5.99±0.01	-6.12±0.01	-6.87 ± 0.01	-7.00 ± 0.0
NGC 4388 (*)		6.86	1.1	44.79	-5.96±0.01	-6.09±0.01		

Note: Column (1): Source name (12 possible disk-masers are in bold text). Column (2): The average stellar velocity dispersion (in units of km s^{-1}) from HypeLeda (<http://leda.univ-lyon1.fr/>). Additionally, the average stellar velocity dispersion for UGC3789 is taken from [Greene et al. \(2016\)](#) and for Mrk1210, NGC2979, Mrk34, NGC5256, NGC5056 & NGC6926 are taken from [Su et al. \(2008\)](#) and [Wang et al. \(2010\)](#). Column (3): Blackhole mass, in units of M_{\odot} , derived from the empirical M - σ relation. For comparison, the dynamical BH mass value for those seven disk-megamaser sources ([Greene et al. 2010, 2016](#)) are also presented (with * symbol). Column (4): Apparent luminosity of maser emission (in units of L_{\odot}), taken from [Tarchi et al. \(2011\)](#), [Bennert et al. \(2009\)](#), [Greenhill et al. \(2008\)](#), and [Darling et al. \(2008\)](#). Column (5): The Eddington luminosities (Eq. 4) derived from estimating the BH mass, in units of ergs^{-1} . Columns (6) & (7): The Eddington ratio \dot{m} derived from the luminosities at 11 cm and 6.0 cm. Columns (8) & (9): The mass accretion rates \dot{M} derived from the luminosities at 11 cm and 6.0 cm, in units of $M_{\odot} \text{yr}^{-1}$. (*): For eight sources: UGC3789, NGC1068, NGC1320, NGC2273, NGC3079, NGC3393, NGC4258, NGC4388, the Eddington ratio \dot{m} are also derived from BH mass results taken from [Greene et al. \(2016\)](#).

Astrophysics, 538, A152

This paper has been typeset from a \LaTeX file prepared by the author.

Table 7. The Parameters of Seyfert 2s without H_2O maser detections

Source	σ	$\log M_{\text{BH}}$	UL- H_2O	$\log L_{\text{Edd}}$	$\log \dot{m}_{11}$	$\log \dot{m}_{6.0}$	$\log \dot{M}_{11}$	$\log \dot{M}_{6.0}$
NGC 777	314	8.96	1.2	47.07	<-8.53	<-8.44	<-7.16	<-7.07
NGC 1058	48	5.31	-0.1	43.42	<-6.68	-7.04 \pm 0.1	<-8.96	-9.32 \pm 0.1
NGC 1358	213	8.2	0.6	46.31	<-7.98	<-8.02	<-7.37	<-7.41
NGC 1667	170	7.76	1.1	45.87	-7.07 \pm 0.02	-7.22 \pm 0.03	-6.9 \pm 0.02	-7.05 \pm 0.03
NGC 2655	160	7.65	0.2	45.76	-7.47 \pm 0.03	-7.5 \pm 0.01	-7.41 \pm 0.03	-7.44 \pm 0.01
NGC 2992	160	7.65	0.1	45.76	-6.98 \pm 0.01	-6.96 \pm 0.01	-6.92 \pm 0.01	-6.89 \pm 0.01
NGC 3147	225	8.31	0.7	46.42	-7.96 \pm 0.01	-7.89 \pm 0.01	-7.24 \pm 0.01	-7.17 \pm 0.01
NGC 3185	76	6.2	-0.2	44.31	<-6.81	<-6.76	<-8.2	<-8.15
NGC 3976	191	7.99	1.1	46.10	-	-7.86 \pm 0.06	-	-7.46 \pm 0.06
NGC 3982	70	6.04	-0.4	44.15	-6.6 \pm 0.02	-6.51 \pm 0.03	-8.15 \pm 0.02	-8.05 \pm 0.03
NGC 4138	126	7.18	-0.5	45.29	-6.27 \pm 0.02	-6.65 \pm 0.01	-6.67 \pm 0.02	-7.06 \pm 0.01
NGC 4168	180	7.88	0.3	45.99	<-8.75	-8.74 \pm 0.05	<-8.46	-8.45 \pm 0.05
NGC 4395	30	4.4	-1.4	42.51	-6.19 \pm 0.05	<-6.68	-9.38 \pm 0.05	<-9.87
NGC 4472	281	8.74	0.4	46.85	-8.71 \pm 0.01	-8.7 \pm 0.01	-7.56 \pm 0.01	-7.55 \pm 0.01
NGC 4501	167	7.73	-0.4	45.84	-7.68 \pm 0.01	-7.79 \pm 0.01	-7.54 \pm 0.01	-7.64 \pm 0.01
NGC 4565	150	7.52	-0.7	45.63	-8.44 \pm 0.01	-8.58 \pm 0.02	-8.51 \pm 0.01	-8.65 \pm 0.02
NGC 4579	165	7.71	-0.4	45.82	-7.79 \pm 0.01	-7.65 \pm 0.01	-7.67 \pm 0.01	-7.53 \pm 0.01
NGC 4594	231	8.36	0.4	46.47	-8.37 \pm 0.01	-8.04 \pm 0.01	-7.6 \pm 0.01	-7.27 \pm 0.01
NGC 4725	132	7.27	-0.5	45.38	<-8.12	<-8.27	<-8.44	<-8.59
NGC 4941	98	6.7	-0.4	44.81	<-7.24	<-7.52	<-8.13	<-8.41
NGC 5005	172	7.79	0.4	45.90	-7.71 \pm 0.01	-7.74 \pm 0.01	-7.51 \pm 0.01	-7.54 \pm 0.01
NGC 5395	146	7.47	0.7	45.58	-6.99 \pm 0.01	-7.07 \pm 0.02	-7.11 \pm 0.01	-7.19 \pm 0.02
NGC 5899	-	-	-	-	-	-	-	-
NGC 6951	115	7.01	-0.1	45.12	-7.13 \pm 0.02	-7.17 \pm 0.02	-7.71 \pm 0.02	-7.74 \pm 0.02
NGC 7743	85	6.42	0.0	44.53	<-6.92	<-6.7	<-8.09	<-7.87

Note: Column (1): Source name. Column (2): The same as Col.(2) in Table.6. For source NGC 5899, the average stellar velocity dispersion is not available. Column (3): Blackhole mass, in the units of M_{\odot} , derived from the empirical M - σ relation. Column (4): The same as Col.(5) in Table.5. Columns (5) to (9): The same as Cols.(5) to (9) in Table.6.